Faraday Discussions

Cite this: *Faraday Discuss.*, 2021, **225**, 271

PAPER

The micromechanical model to computationally investigate cooperative and correlated phenomena in metal–organic frameworks†

Sven M. J. Rogge *

Received 30th December 2019, Accepted 15th January 2020
DOI: 10.1039/c9fd00148d

Computational insight into the impact of cooperative phenomena and correlated spatial disorder on the macroscopic behaviour of metal–organic frameworks (MOFs) is essential in order to consciously engineer these phenomena for targeted applications. However, the spatial extent of these effects, ranging over hundreds of nanometres, limits the applicability of current state-of-the-art computational tools in this field. To obtain a fundamental understanding of these long-range effects, the micromechanical model is introduced here. This model overcomes the challenges associated with conventional coarse-graining techniques by exploiting the natural partitioning of a MOF material into unit cells. By adopting the elastic deformation energy as the central quantity, the micromechanical model hierarchically builds on experimentally accessible input parameters that are obtained from atomistic quantum mechanical or force field simulations. As a result, the here derived micromechanical equations of motion can be adopted to shed light on the effect of long-range cooperative phenomena and correlated spatial disorder on the performance of mesoscale MOF materials.

1 Introduction

Thanks to the peculiar and highly porous structures of metal–organic frameworks (MOFs),[1–3] composed of organic and inorganic building blocks,[4] these materials often exhibit 'anomalous' and highly cooperative responses to external stimuli.[5] These peculiar phenomena, such as negative gas adsorption,[6] exceptionally high elastic anisotropy,[7] or even the emergence of multiple metastable phases and large-amplitude structural flexibility,[8–10] arise from the large diversity of interaction strengths in MOFs.[11] Computational research provides an essential tool to understand how these fundamental interactions at the atomic scale, varying from

Center for Molecular Modeling, Ghent University, Technologiepark 46, Zwijnaarde, 9052, Belgium. E-mail: Sven.Rogge@UGent.be

† Electronic supplementary information (ESI) available: Derivation of the micromechanical equations of motion for unistable and bistable nanocells. See DOI: 10.1039/c9fd00148d

strong covalent bonds over weaker coordination bonds to weak but long-range dispersion interactions, ultimately combine to result in the observed macroscopic behaviour of MOFs.[12,13] Two competing ingredients are essential to accurately model the macroscopic behaviour of these materials.[14] On the one hand, the adopted model needs to capture the diversity of interactions that give rise to the MOF's macroscopic response to external stimuli. On the other hand, the adopted model should also be able to cover sufficiently large regions of the MOF material, so that possible cooperative behaviour can be adequately represented. For instance, to shed light on the experimental observation that flexible MOFs tend to become more rigid upon decreasing the crystallite size to the submicrometre regime,[15–20] computer models need to capture the long-range phenomena that occur on length scales on the order of the crystal size.

In this respect, quantum mechanical methods are most accurate but are often too computationally expensive to dynamically simulate MOF systems larger than a few nanometres.[21,22] By approximating the atomic interactions by analytical functions, system-specific force fields can dynamically model much larger systems at the expense of a reduction in accuracy.[23–26] Recently, MOF models with dimensions of up to 10–20 nm and containing up to a few tens of thousands of atoms were investigated using these force fields, revealing that flexible MOFs can exhibit phase coexistence under external stimuli.[27,28] This phase coexistence, a type of correlated spatial disorder in which multiple (meta)stable phases coexist in the material at the same time, provides a possible explanation for the experimentally observed size effect as it decreases the barrier for the switchable behaviour of flexible MOFs, but can only be observed when considering sufficiently large models.[28] However, even system-specific force fields, either at the atomic or the coarse-grained level,[29] are unable to directly model systems at length scales corresponding to the experimental crystal size and investigate cooperative phenomena that extend over the whole crystal. Therefore, the micromechanical model is introduced in this article as a hierarchical coarse-grained model that goes beyond system-specific force fields to capture these long-range cooperative effects while still approximating sufficiently well the variety of interactions present in MOFs.

The need for computational models capable of describing larger MOF structures is not only inspired by the aim to understand their cooperative macroscopic responses to external stimuli. In recent years, awareness has grown that MOFs are not the perfectly crystalline materials once envisioned, but that they exhibit inherent spatial disorder that strongly impacts their macroscopic behaviour. As indicated in Fig. 1, inherent spatial disorder in MOFs may be classified according to its spatial extent, ranging from short-range isolated disorder up to a few nanometres, over mid-range correlated disorder up to a few tens of nanometres, to long-range correlated disorder on even larger length scales and involving up to several millions of atoms. The most prominent examples of short-range disorder in MOFs are point defects, such as the linker and node vacancies in UiO-66 and HKUST-1,[30–33] shown in Fig. 1(a), and the under-coordinated metal sites in MIL-53(Al,V).[34] In larger concentrations, these defects are observed to conglomerate into correlated nanoregions, such as in UiO-66,[32,35] or to form mesopores, as in HKUST-1,[36,37] giving rise to mid-range spatial disorder extending over several nanometres (Fig. 1(b)). Finally, MOFs may also exhibit long-range correlated disorder, in which large parts of the crystal cooperatively undergo phase

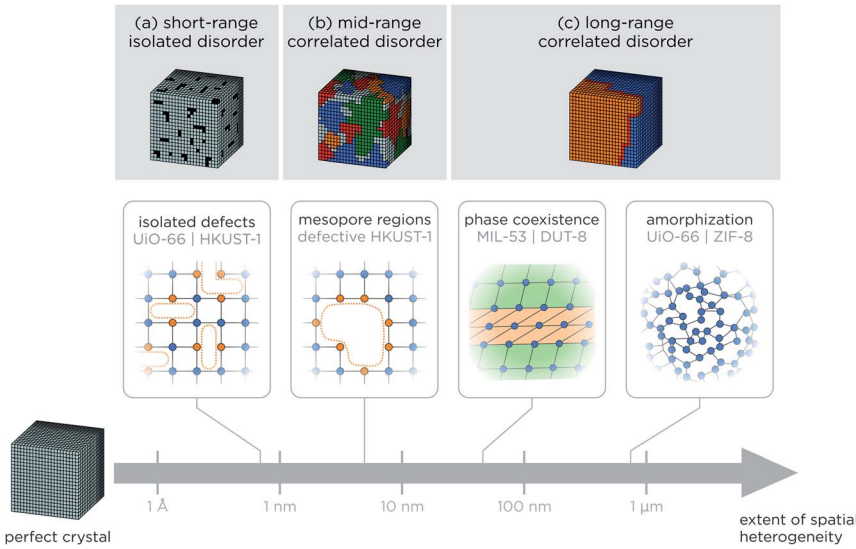

Fig. 1 Classification of the different types of spatial disorder observed in MOFs and related materials, varying from (a) short-range isolated disorder (< *ca.* 1 nm), over (b) mid-range correlated disorder (*ca.* 1–20 nm), to (c) long-range correlated disorder (> *ca.* 20 nm) with selected examples for each of the different types of spatial disorder.

transitions between different metastable phases, potentially giving rise to phase coexistence (Fig. 1(c)).[27,28] These transitions may be triggered not only between two crystalline phases, such as for MIL-53 or DUT-8,[38,39] but also from a crystalline to an amorphous phase. The latter phenomenon, termed amorphization, has been observed in UiO-66 and various zeolitic imidazolate frameworks (ZIFs),[40,41] among others, and results in the formation of amorphous MOFs (aMOFs) or liquid MOFs that retain the connectivity of the parent material while exhibiting strongly altered properties.[42–44]

As spatial disorder profoundly affects the MOF's macroscopic behaviour, the intentional creation of defects—so-called defect engineering—has emerged as a promising concept to synthesise spatially disordered MOFs with improved performance in, *e.g.*, heterogeneous catalysis and gas adsorption.[22,45–47] Although defect engineering mainly focuses on the targeted creation of isolated defects, correlated spatial disorder has an even vaster potential to revolutionise the design of MOFs as functional devices.[48] However, a fundamental understanding of the impact of correlated spatial disorder on the performance of MOFs requires computational techniques that can model these spatially extended systems with sizes of up to a few hundreds of nanometres.[14]

To investigate these mid- and long-range cooperative phenomena that fall beyond the reach of current computational models, the micromechanical model is introduced in this work. By combining a substantial reduction in the degrees of freedom of the MOF material with specific interaction terms that capture the MOF's flexibility, this model enables the direct simulation of long-range cooperative effects and correlated spatial disorder. As the micromechanical model builds on experimentally verifiable quantities that can be extracted from system-

specific force fields or *ab initio* data, it can be adopted as an integrated and hierarchical approach connecting higher-level simulations with experiments. As a result, the here introduced micromechanical model forms a computational framework to shed light on the various cooperative phenomena taking place in MOFs, spanning the different length scales from the sub-nanometre to the micrometre regime.

2 The micromechanical concept

While coarse-graining techniques have already been used extensively for biomolecular and polymer systems,[49–51] specific challenges arise when trying to adopt these techniques for periodic network materials such as MOFs.[29,52] Section 2.1 outlines how these traditional techniques pose non-trivial limitations for the coarse-grained description of MOFs, leading to the formulation of the micromechanical model. Similar to conventional coarse-graining procedures, the computational speed-up of the micromechanical model is achieved by reducing the number of interaction beads on the one hand and approximating the interactions between these beads by relatively simple analytical functions on the other hand. As shown schematically in Fig. 2, the micromechanical model consists of three steps. The first step consists of mapping the atomistic representation of the MOF on a suitable coarse-grained representation that exploits the natural partitioning of the material in similar unit cells, as outlined in Section 2.2. In the second step, atomistic simulations are performed, either at the *ab initio* or the force field level, to parametrise the coarse-grained interactions. Finally, in the third step, the coarse-grained material is propagated in time using the equations of motion derived in Sections 2.3 and 2.4 for systems that can be described by a single phase, *e.g.*, to derive the properties near equilibrium, and for systems that exhibit multiple phases, respectively.

2.1 Challenges in coarse-graining MOFs

Martini-like coarse-graining approaches, in which up to four non-hydrogen atoms are collected into a single bead, are traditionally adopted when coarse-graining

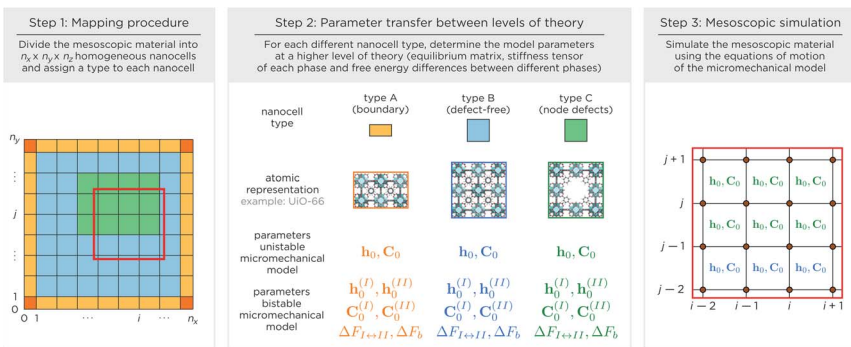

Fig. 2 The three steps in the micromechanical model, illustrated for UiO-66 containing nodal defect regions (green), defect-free regions (blue) and surface regions (orange). Step 3 shows a close-up of the model for the region defined by the red rectangle in step 1.

biomolecules or polymer systems.[53] While this procedure has proven effective for isolated systems and has been used to coarse-grain guests in MOFs, it is not straightforward to extend this approach to the MOF network itself. Specifically, four challenges may be identified when trying to construct a Martini-like coarse-graining mapping procedure for extended network materials such as MOFs.

The first challenge results from the often highly symmetric organic and inorganic building blocks of MOFs, which restrict the freedom in symmetry-preserving coarse-grained mapping procedures. For instance, consider the $Zr_6(\mu_3\text{-}OH)_4(\mu_3\text{-}O)_4$ inorganic node present in the hydroxylated form of UiO-66(Zr),[56] visualised in the inset of Fig. 3. When neglecting the highly disordered hydrogen atoms in the node, this building block satisfies the octahedral O_h point group containing 48 symmetry elements. Collecting the atoms of this node into coarse-grained beads necessarily reduces this symmetry or requires atoms to be present in multiple beads, which would lead to inconsistent momentum distributions in the atomistic and coarse-grained representations.[57] The only trivial exceptions are those in which each atom defines its own bead or in which the bead contains the complete inorganic node. A similar observation holds when coarse-graining the phenyl moieties of the organic ligands. As a result, the four-to-one mapping in Martini-like coarse-graining is often not attainable for MOFs. Instead, in the first coarse-grained MOF force field developed by Dürholt *et al.* for HKUST-1,[29,55] a reduction in degrees of freedom of about one order of magnitude was proposed by replacing each of the inorganic nodes and organic ligands by one bead, corresponding to the topology of the material.

The second challenge arises when considering MOFs in which the building blocks are not isolated moieties but rather extend along chains, such as the $[Al(\mu_2\text{-}OH)]_n$ chain of MIL-53(Al) (see inset of Fig. 3).[54] In such a case, it is non-trivial to partition the atoms into coarse-grained beads. In MIL-53(Al), for instance, the μ_2-OH group is connected to two equivalent aluminium atoms. As a result, when assigning this hydroxyl group to either one of the neighbouring aluminium atoms, the symmetry would be reduced, similar to the first challenge for highly symmetric nodes such as in UiO-66. However, while this could be circumvented in

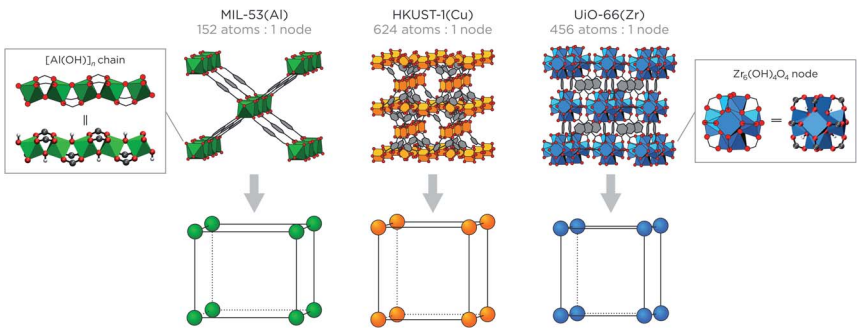

Fig. 3 The micromechanical procedure to map the atomistic model onto the nanocells for three representative MOFs, MIL-53(Al),[54] HKUST-1(Cu),[55] and UiO-66(Zr),[56] with the corresponding reduction in the number of degrees of freedom. Insets show the atomistic representations of the inorganic moieties in MIL-53(Al) (left) and UiO-66(Zr) (right). Colour code: zirconium (blue), copper (orange), aluminium (green), oxygen (red), carbon (grey) and hydrogen (white). Hydrogen atoms are omitted from the periodic materials for clarity.

UiO-66 by considering the whole node as a single bead, this is not possible for MIL-53(Al) as the bead would have to extend along the whole $[Al(\mu_2\text{-}OH)]_n$ chain.

The third challenge is rooted in the different types of spatial disorder present in MOFs. As spatial disorder results in regions of the material that are similar but not identical, it limits the transferability of traditional mapping procedures. For instance, UiO-66 is prone to linker and node defects, affecting the coordination of the inorganic nodes that remain in the material.[30–32,35] Even when considering minimally defective UiO-66 MOFs, with an average node coordination number of eleven, and assuming no capping molecules are present to replace the missing ligands, up to seven different inorganic nodes that give rise to this average coordination number can be constructed.[58] While these nodes all contain six zirconium atoms, their direct atomistic environments differ. Despite the chemical similarity between these nodes, coarse-grained mapping procedures that define *a priori* how many atoms should be collected in coarse-grained beads would give rise to distinct mappings. Even when the mapping procedure would allow for flexibility in the number of atoms per bead, the interactions between these beads would need to be defined for each similar node separately. In both cases, the transferability of the coarse-grained model would be hampered.

The fourth and final challenge, which is the main impetus for the micromechanical model, is that the length scale attainable by state-of-the-art coarse-grained models for MOFs is still limited to a few tens of nanometres.[29] This results from the fact that even the coarsest MOF models used up to now achieve a reduction in the number of beads of about one order of magnitude.[29,52] To describe cooperative phenomena or correlated disorder that go beyond a few tens of nanometres, however, a fundamentally different coarse-graining procedure with a further reduction in the number of beads is necessary.[14]

2.2 The nodal micromechanical mapping procedure

To address the four challenges mentioned above, the first step in the micromechanical model is to define a mapping that reduces the number of interaction beads by two to three orders of magnitude (see step 1 in Fig. 2). This is achieved by observing that mesoscopic MOF crystals, with dimensions of several hundreds of nanometres and containing several millions of atoms, can be easily partitioned into smaller unit cells with dimensions of about one nanometre given the MOF's building block structure. These nanosized unit cells, which will be further referred to as nanocells, are defined by the position of their eight corners (in 3D). In the micromechanical model, the position of these corners, which define the coarse-grained nodes of the model, will be simulated. As indicated in Fig. 3 for three representative MOFs, the mapping of the atomistic unit cells to coarse-grained nodes achieves the targeted reduction in degrees of freedom of more than two orders of magnitude.

To illustrate this mapping procedure, consider the mesoscopic material shown in step 1 of Fig. 2. For this 2D material, the nodes are indexed with a couple of integers (i,j), ranging from $(0, 0)$ to (n_x, n_y). These nodes are characterised by their position $\boldsymbol{r}_{ij}$ and mass m_{ij}, which is determined based on the average mass of the surrounding nanocells. In turn, these nodes uniquely define the positions of the different nanocells $\mathbf{h}_{\mu\nu}$, as outlined in Section S1.1 of the ESI.† In the model, the nodes at the boundaries of the mesoscopic material can either be free, mimicking

finite materials, or they can be coupled through periodic boundary conditions, mimicking the bulk region of an even larger material.

Next, a nanocell type is assigned to each nanocell in the material, indicated with the different colors in Fig. 2. This nanocell type is uniquely defined by the spatial disorder present in or at the surface of the nanocell. The nanocell type will remain unaltered during the simulation, given that classical simulations do not allow for bonds to be broken or formed. However, as outlined in more detail in Section 2.4, these nanocell types can dynamically switch between multiple phases as long as all bonds remain intact during the transition. For instance, different nanocell types could be assigned to the different defective nanoregions in UiO-66, such as the single green nanodefect region in Fig. 2. Likewise, surfaces can be described by identifying surface nanocell types, such as those indicated by the two shades of orange in Fig. 2. These surfaces can be external, to describe the finite crystal size, or internal, to describe mesopores. The number of nanocell types, typically smaller than ten, determines the complexity of the micromechanical model and the number of atomistic simulations needed to parametrise the model, as outlined in Section 2.3.

2.3 The micromechanical equations of motion for unistable nanocells

Atomistically, external stimuli and spatial disorder in MOFs result in distorted nanocells. The assumption made in the micromechanical model is that this altered performance at the atomistic level can be used to characterise the nodal interactions near equilibrium. Consequently, the parameters of the micromechanical model are the 3×3 equilibrium cell matrices $\mathbf{h}_{\mu\nu\kappa,0}$ and the fourth-order $3 \times 3 \times 3 \times 3$ stiffness tensors $\mathbf{C}_{\mu\nu\kappa,0}$ for each of the nanocells in the model. Both the equilibrium cell matrices and the stiffness tensors can be *a priori* determined from atomistic simulations,[59] which need to be performed for each different nanocell type (step 2 in Fig. 2). These parameters can be used to define the 3×3 finite Lagrangian strain tensor $\boldsymbol{\varepsilon}_{\mu\nu\kappa}$ experienced by the nanocell $\mathbf{h}_{\mu\nu\kappa}$ as

$$\boldsymbol{\varepsilon}_{\mu\nu\kappa} = \frac{1}{2}\left[\mathbf{h}_{\mu\nu\kappa,0}^{-\mathrm{T}}\mathbf{h}_{\mu\nu\kappa}^{\mathrm{T}}\mathbf{h}_{\mu\nu\kappa}\mathbf{h}_{\mu\nu\kappa,0}^{-1} - \mathbf{1}\right], \tag{1}$$

in which $\mathbf{1}$ is the 3×3 unit tensor.[60] In turn, this leads to the following elastic potential energy associated with each of the nanocells:

$$\mathscr{U}_{\mu\nu\kappa} = \frac{1}{2}\det(\mathbf{h}_{\mu\nu\kappa})\boldsymbol{\varepsilon}_{\mu\nu\kappa}^{\mathrm{T}}\colon \mathbf{C}_{\mu\nu\kappa,0}\colon \boldsymbol{\varepsilon}_{\mu\nu\kappa}. \tag{2}$$

In this expression, ':' denotes the double contraction operator:

$$\left[\boldsymbol{\varepsilon}^{\mathrm{T}}\colon \mathbf{C}\right]_{k\ell} = \sum_{i=1}^{3}\sum_{j=1}^{3}\varepsilon_{ji}C_{ijk\ell} \text{ and } \left[\mathbf{C}\colon \boldsymbol{\varepsilon}\right]_{k\ell} = \sum_{i=1}^{3}\sum_{j=1}^{3}C_{k\ell ij}\varepsilon_{ij}. \tag{3}$$

As outlined in Section S1.2 of the ESI,† this elastic deformation energy naturally leads to the following Hamiltonian for the micromechanical model:

$$\mathscr{H}(\boldsymbol{r},\boldsymbol{p}) = \sum_{ijk}\frac{\boldsymbol{p}_{ijk}^{2}}{2m_{ijk}} + \sum_{\mu\nu\kappa}\mathscr{U}_{\mu\nu\kappa}(\boldsymbol{r}), \tag{4}$$

where $\boldsymbol{p}_{ijk}$ is the conjugated momentum of the node at position $\boldsymbol{r}_{ijk}$.

From this Hamiltonian, the equations of motion can be derived as

$$\dot{\boldsymbol{r}}_{ijk} = \nabla_{\boldsymbol{p}_{ijk}}\mathscr{H} = \frac{\boldsymbol{p}_{ijk}}{m_{ijk}} = \boldsymbol{v}_{ijk}, \tag{5}$$

$$\dot{\boldsymbol{p}}_{ijk} = -\nabla_{\boldsymbol{r}_{ijk}}\mathscr{H} = -\sum_{\mu=i-1}^{i}\sum_{\nu=j-1}^{j}\sum_{\kappa=k-1}^{k}\nabla_{\boldsymbol{r}_{ijk}}\mathscr{U}_{\mu\nu\kappa}(\boldsymbol{r}). \tag{6}$$

As outlined in Sections S1.3 and S1.4 of the ESI,† eqn (6) can be written out explicitly, yielding for instance for the x-component of the conjugated momentum of the node at position (i, j, k):

$$\dot{p}_{ijk,x} = -\frac{1}{2}\sum_{\mu=i-1}^{i}\sum_{\nu=j-1}^{j}\sum_{\kappa=k-1}^{k}\det(\mathbf{h}_{\mu\nu\kappa})\times\left[\mathrm{Tr}\left\{\mathbf{h}_{\mu\nu\kappa}^{-1}\frac{\partial}{\partial x_{ijk}}\mathbf{h}_{\mu\nu\kappa}\right\}\boldsymbol{\varepsilon}_{\mu\nu\kappa}^{\mathrm{T}}\colon\mathbf{C}_{\mu\nu\kappa,0}\colon\boldsymbol{\varepsilon}_{\mu\nu\kappa}\right.$$
$$\left.+\frac{1}{32}\left(\mathbf{h}_{\mu\nu\kappa,0}^{-\mathrm{T}}\mathbf{F}_{n_{\mu\nu\kappa},x}\mathbf{h}_{\mu\nu\kappa,0}^{-1}\right)\colon\mathbf{C}_{\mu\nu\kappa,0}\colon\boldsymbol{\varepsilon}_{\mu\nu\kappa}+\frac{1}{32}\boldsymbol{\varepsilon}_{\mu\nu\kappa}^{\mathrm{T}}\colon\mathbf{C}_{\mu\nu\kappa,0}\colon\left(\mathbf{h}_{\mu\nu\kappa,0}^{-\mathrm{T}}\mathbf{F}_{n_{\mu\nu\kappa},x}\mathbf{h}_{\mu\nu\kappa,0}^{-1}\right)\right]. \tag{7}$$

In this expression, $\mathrm{Tr}\{\mathbf{A}\}$, $\mathbf{A}^{-1}$, and $\mathbf{A}^{\mathrm{T}}$ are the trace, the inverse, and the transpose of matrix $\mathbf{A}$, respectively, and $\mathbf{A}^{-\mathrm{T}} = (\mathbf{A}^{-1})^{\mathrm{T}}$. The matrix $\mathbf{F}_{n_{\mu\nu\kappa},x}$, with elements

$$\mathbf{F}_{n_{\mu\nu\kappa},x} = \begin{bmatrix} 2f_{n_{\mu\nu\kappa}} & f_{n_{\mu\nu\kappa}} & f_{n_{\mu\nu\kappa}} \\ f_{n_{\mu\nu\kappa}} & 0 & 0 \\ f_{n_{\mu\nu\kappa}} & 0 & 0 \end{bmatrix}, \tag{8}$$

contains one of the functions f_1 to f_8, corresponding to the contribution of each of the eight neighbouring nanocells $\mathbf{h}_{\mu\nu\kappa}$ that have the node in position (i, j, k) on one of their corners, as expressed by the summation in eqn (6). As outlined in Section S1.3 of the ESI,† f_1 to f_8 are simple linear functions of the coordinates of the 27 nodes that form these eight nanocells, with the node in position (i, j, k) as the central node.

The here obtained equations of motion can be used to dynamically propagate the mesoscale material using the equilibrium cell matrix and the equilibrium stiffness tensor as input parameters (step 3 in Fig. 2), and can be supplemented by thermostats and barostats to achieve temperature and pressure control, respectively, similar to the atomistic equations of motion.[61]

2.4 Extension of the micromechanical model towards bistable nanocells

The micromechanical equations of motion derived in Section 2.3 only take into account the elastic deformation of the material through the elastic deformation energy of eqn (2). While this is sufficient to extract the properties of the mesoscopic material near equilibrium, such as its equilibrium volume, bulk modulus, or thermal expansion, there is growing attention to the anharmonic, out-of-equilibrium responses of MOFs, such as their transition or amorphization pressures. Essential in these out-of-equilibrium phenomena is that the material can undergo a transition between two phases. To capture these effects, the bistability of these materials needs to be directly incorporated in the micromechanical model by considering bistable instead of unistable nanocells.

To describe nanocells that have two (meta)stable phases, information about the deformation energy of the two phases and their relative stability needs to be provided instead of the single deformation energy of eqn (2). As shown in Fig. 4,

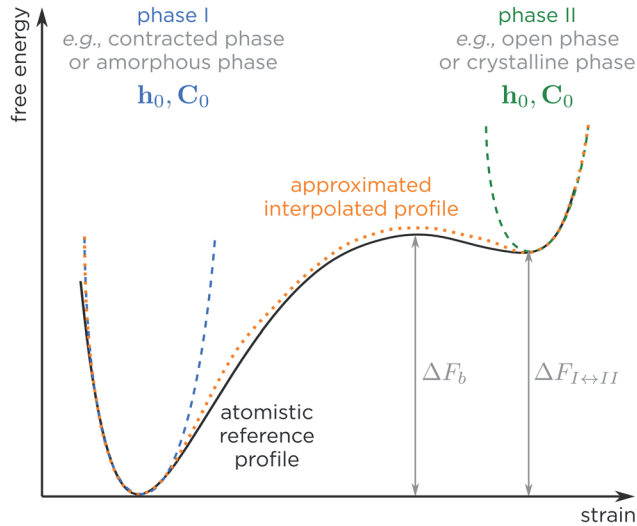

Fig. 4 Visual representation of the procedure to extend the micromechanical model to systems with multiple metastable phases. The two dashed parabolas indicate the harmonic responses of the two phases, I and II, separately, while the orange dotted line is the interpolation obtained according to the procedure in ref. 62.

this information encompasses the equilibrium matrices $\mathbf{h}_{\mu\nu\kappa,0}$ and the stiffness tensors $\mathbf{C}_{\mu\nu\kappa,0}$ of the two phases, I and II, as well as their relative difference in free energy $\Delta F_{\mathrm{I}\leftrightarrow\mathrm{II},\mu\nu\kappa}$ and finally the height of the barrier between the two phases $\Delta F_{b,\mu\nu\kappa}$. Based on this information, the deformation energies $\mathscr{U}^{(\mathrm{I})}_{\mu\nu\kappa}$ and $\mathscr{U}^{(\mathrm{II})}_{\mu\nu\kappa}$ of the two phases can be determined separately *via* eqn (1), yielding the harmonic equilibrium response for both phases as shown in Fig. 4. To combine these two potential energies into an interpolated potential energy that spans both phases of the bistable nanocell, the approach of Christ and van Gunsteren is adopted,[62] yielding the following potential energy surface for the bistable nanocell $\mathbf{h}_{\mu\nu\kappa}$:

$$\mathscr{U}_{\mu\nu\kappa} = -k_{\mathrm{B}} T^*_{\mu\nu\kappa} \ln\left[\exp\left(-\frac{\mathscr{U}^{(\mathrm{I})}_{\mu\nu\kappa}}{k_{\mathrm{B}} T^*_{\mu\nu\kappa}}\right) + \exp\left(-\frac{\mathscr{U}^{(\mathrm{II})}_{\mu\nu\kappa} + \Delta F_{\mathrm{I}\leftrightarrow\mathrm{II},\mu\nu\kappa}}{k_{\mathrm{B}} T^*_{\mu\nu\kappa}}\right)\right]. \quad (9)$$

In this expression, k_{B} is the Boltzmann constant and $T^*_{\mu\nu\kappa}$ is an effective temperature that determines the smoothness of the interpolation. In practice, the parameter $T^*_{\mu\nu\kappa}$ should be fitted to best reproduce the barrier $\Delta F_{b,\mu\nu\kappa}$ obtained from atomistic simulations.

The updated equations for the positions of the nodes of unistable nanocells, eqn (5), remain unaltered when considering bistable nanocells. For the momenta of the nodes, eqn (6), the derivatives $-\nabla_{\boldsymbol{r}_{ijk}} \mathscr{U}_{\mu\nu\kappa}(\boldsymbol{r})$ depend on whether the nanocell $\mathbf{h}_{\mu\nu\kappa}$ is unistable, as in Section 2.3, or bistable. As outlined in Section S2 of the ESI,† the derivative of the bistable potential energy is a weighted linear combination of the derivatives of the two single-phase deformation potential energies:

$$\nabla_{\boldsymbol{r}_{ijk}} \mathscr{U}_{\mu\nu\kappa}(\boldsymbol{r}) = w^{(\mathrm{I})}_{\mu\nu\kappa}(\boldsymbol{r}) \nabla_{\boldsymbol{r}_{ijk}} \mathscr{U}^{(\mathrm{I})}_{\mu\nu\kappa}(\boldsymbol{r}) + w^{(\mathrm{II})}_{\mu\nu\kappa}(\boldsymbol{r}) \nabla_{\boldsymbol{r}_{ijk}} \mathscr{U}^{(\mathrm{II})}_{\mu\nu\kappa}(\boldsymbol{r}), \quad (10)$$

with weight factors

$$w^{(\mathrm{I})}_{\mu\nu\kappa}(\boldsymbol{r}) = \frac{\exp\left(-\dfrac{\mathscr{U}^{(\mathrm{I})}_{\mu\nu\kappa}(\boldsymbol{r})}{k_\mathrm{B}T^*_{\mu\nu\kappa}}\right)}{\exp\left(-\dfrac{\mathscr{U}^{(\mathrm{I})}_{\mu\nu\kappa}(\boldsymbol{r})}{k_\mathrm{B}T^*_{\mu\nu\kappa}}\right) + \exp\left(-\dfrac{\mathscr{U}^{(\mathrm{II})}_{\mu\nu\kappa}(\boldsymbol{r}) + \Delta F_{I\leftrightarrow II,\mu\nu\kappa}}{k_\mathrm{B}T^*_{\mu\nu\kappa}}\right)}; \tag{11}$$

$$w^{(\mathrm{II})}_{\mu\nu\kappa}(\boldsymbol{r}) = \frac{\exp\left(-\dfrac{\mathscr{U}^{(\mathrm{II})}_{\mu\nu\kappa}(\boldsymbol{r}) + \Delta F_{\mathrm{I}\leftrightarrow\mathrm{II},\mu\nu\kappa}}{k_\mathrm{B}T^*_{\mu\nu\kappa}}\right)}{\exp\left(-\dfrac{\mathscr{U}^{(\mathrm{I})}_{\mu\nu\kappa}(\boldsymbol{r})}{k_\mathrm{B}T^*_{\mu\nu\kappa}}\right) + \exp\left(-\dfrac{\mathscr{U}^{(\mathrm{II})}_{\mu\nu\kappa}(\boldsymbol{r}) + \Delta F_{\mathrm{I}\leftrightarrow\mathrm{II},\mu\nu\kappa}}{k_\mathrm{B}T^*_{\mu\nu\kappa}}\right)}. \tag{12}$$

Compared to the unistable case, bistable nanocells will hence require two evaluations of the derivative of the potential energy, $\nabla_{\boldsymbol{r}_{ijk}}\mathscr{U}^{(\mathrm{I})}_{\mu\nu\kappa}(\boldsymbol{r})$ and $\nabla_{\boldsymbol{r}_{ijk}}\mathscr{U}^{(\mathrm{II})}_{\mu\nu\kappa}(\boldsymbol{r})$, at every time step. As in the unistable case, however, all required input parameters—the equilibrium cell matrices, the stiffness tensors, the relative free energy difference, and the free energy barrier between the phases—are obtained from *a priori* atomistic simulations and need to be derived only for the different nanocell types, again limiting the complexity of the model.

3 Discussion

The micromechanical model introduced here follows a fundamentally different approach to coarse-graining MOFs compared to traditional coarse-graining techniques, exploiting the natural partitioning of the MOF material in similar nanocells. The three main differences between the micromechanical model and conventional coarse-grained force fields are highlighted by the equations of motion derived in Sections 2.3 and 2.4.

First, even though the micromechanical model adopts a coarse mapping procedure that is very similar for all MOFs, information about the topology of the atomistic material is still partially contained in the equilibrium cell matrices and the stiffness tensors. This is a deliberate choice, as the topology of the material was found to be an indispensable factor to accurately predict the structural and mechanical responses of MOFs to external stimuli.[63,64]

Second, the interactions in the micromechanical model are not restricted to nearest-neighbour beads, but include *via* eqn (8) interactions with all neighbouring beads that share at least one nanocell. This increases the complexity of the model compared to conventional coarse-graining techniques, although the functional form of the interactions remains simple and the mapping procedure already introduces a substantial reduction in complexity.

Third, the parameters that are used as input for the micromechanical model—equilibrium cell matrices and equilibrium stiffness tensors, possibly extended by differences in free energy in the case of bistable nanocells—are well-defined variables that can, to a large extent, be obtained experimentally. This contrasts with the often arbitrary analytical interaction terms used in conventional coarse-grained force fields, for which the accuracy of the interaction terms can only be determined *a posteriori* by comparing the results predicted by the coarse-grained model with experimental results. Even then, if a mismatch with experiment is

obtained, it is often not trivial to pinpoint which interaction terms are missing or which terms need to be refined to improve the accuracy of conventional coarse-graining procedures. In contrast, in the micromechanical model, the input parameters can be *a priori* compared with experiment. Furthermore, if higher-level force field or quantum mechanical information would be challenging to obtain, these input parameters can also be directly extracted from experiment.

As a result of the specific approach followed in the micromechanical model, the four challenges outlined in Section 2.1 can be addressed. As visualised in Fig. 3, the micromechanical model maps the unit cell of the material, with a given space group, on its crystal system instead of mapping the different atoms inside the cell onto arbitrary coarse-grained beads as in conventional coarse-graining techniques. Conceptually, the reduction of the unit cell to its crystal system can be regarded as the periodic analogon of reducing the isolated building blocks in the material to their point group. As a result of this specific mapping procedure, the micromechanical model does not require the atomistic building blocks to be partitioned in different beads, circumventing the challenges related to highly symmetric building blocks, such as the $Zr_6(\mu_3\text{-}OH)_4(\mu_3\text{-}O)_4$ inorganic node in UiO-66(Zr), and building blocks that extend along chains, such as the $[Al(\mu_2\text{-}OH)]_n$ chain in MIL-53(Al). Moreover, as the different nodes in the micromechanical model can move independently, the crystal system of any given nanocell can change during the simulation, which is a prerequisite in modelling phase transitions.

Furthermore, nanocells that are structurally and mechanically similar will be characterised by nanocell types that have similar equilibrium cell matrices and equilibrium stiffness tensors. Combined with the straightforward mapping procedure in Fig. 3, this ensures that the micromechanical model is easily transferable between different MOFs or between MOFs containing various types of spatial disorder, overcoming the third challenge in Section 2.1. As a result, the micromechanical model can be adopted to investigate possible cooperative effects that arise from multiple types of spatial disorder being present in the material at the same time, such as the combination of node defects and boundary effects present in the hypothetical UiO-66 material in Fig. 2. In addition, the model can also describe hybrid materials in which a given MOF is dispersed into a different MOF matrix, such as the recently synthesised MIL-53/ZIF-62 hybrid.[65]

Finally, the gain in attainable length scale in the micromechanical model is expected to be substantially larger than for atomistic or conventional coarse-grained MOF models, due to three factors. First, the mapping procedure results in a reduction in degrees of freedom of two to three orders of magnitude with respect to atomistic models, thereby going beyond the reductions achieved by state-of-the-art coarse-grained MOF models.[29,52] In addition, the Hamiltonian of the micromechanical model, expressed in eqn (4), is smoother than the atomistic Hamiltonian, as it no longer contains atomistic high-frequency modes such as O–H and C–H stretches. As a result, the time step used during a molecular dynamics simulation with the micromechanical model can be about one order of magnitude larger than in the atomistic case without violating the Nyquist theorem. Finally, due to the absence of long-range interactions, the force evaluations in the micromechanical model will be faster than in the atomistic case. As a result, the micromechanical model has the potential to computationally describe

cooperative phenomena and correlated spatial disorder at length scales beyond the few tens of nanometres achievable today.

The micromechanical model relies on the partitioning of the material in nanocells and the determination of the equilibrium cell matrices and stiffness tensors of these nanocells. While this is a natural approach for largely crystalline MOFs, it becomes less straightforward to define these parameters when considering glassy or amorphous materials.[44] This is for instance the case when describing the amorphization of UiO-66(Zr), in which phase I in Fig. 4 corresponds to an amorphous phase next to the crystalline phase II. If we are only interested in the amorphization pressure, *i.e.*, the pressure required to go from phase II to phase I, the exact parametrisation of the amorphous phase can be expected to be less important, as an accurate reproduction of the amorphization pressure of the nanocell only requires information on the crystalline phase and the point at which the structural response of the crystalline material becomes highly anharmonic.[58] As a result, the amorphization pressure of the different nanocells can be captured by fitting the parameters $\Delta F_{\mathrm{I}\leftrightarrow\mathrm{II}}$ and T^* of the model to atomistic data obtained for the nanocell. In addition, given that the input parameters of the model can be determined experimentally, the amorphous phase can also be parametrised based on experiment. In this sense, the micromechanical model may also form a complementary computational tool to help refine the experimental structures of these amorphous or glassy phases based on the experimentally observed macroscopic behaviour of the MOF.[14]

4 Conclusions

Spatially extended computational models are necessary to understand on a fundamental level how the variety of interactions and various types of spatial disorder in MOFs lead to the experimentally observed cooperative phenomena in these materials. However, conventional computational techniques are often inadequate for coarse-graining periodic network materials such as MOFs as they lead to an insufficient increase in length scale that can be described in the model. Therefore, the micromechanical model is introduced here as a fundamentally different coarse-graining approach that exploits the natural partitioning of MOFs into nanometre-sized cells. This model consists of two ingredients: a systematic procedure to map the atomistic unit cells onto coarse-grained nanocells, leading to a reduction in the number of degrees of freedom of about two to three orders of magnitude, and a description of the nodal Hamiltonian that defines the equations of motion to propagate the micromechanical model in time.

Herein, the concept of the micromechanical model is outlined and the equations of motion for both unistable and bistable materials are derived. In contrast to conventional coarse-graining techniques, the model is only based on experimentally verifiable input parameters, which can be determined from higher-level quantum mechanical or force field simulations. As a result, the here proposed micromechanical model can be considered as a hierarchical method that builds upon atomic-level information to predict how cooperative phenomena and correlated spatial disorder affect the performance of mesoscale MOF materials under experimental conditions.

Conflicts of interest

There are no conflicts to declare.

Acknowledgements

This work is supported by the Fund for Scientific Research Flanders (FWO) through a postdoctoral fellowship (grant no. 12T3519N). Fruitful discussions on the concept and the scope of the micromechanical model with Prof. Veronique Van Speybroeck and Prof. Toon Verstraelen are gratefully acknowledged.

References

1 H. Li, M. Eddaoudi, M. O'Keeffe and O. M. Yaghi, *Nature*, 1999, **402**, 276–279.
2 G. Férey, *Chem. Mater.*, 2001, **13**, 3084–3098.
3 S. Kitagawa, R. Kitaura and S.-i. Noro, *Angew. Chem., Int. Ed.*, 2004, **43**, 2334–2375.
4 O. M. Yaghi, M. O'Keeffe, N. W. Ockwig, H. K. Chae, M. Eddaoudi and J. Kim, *Nature*, 2003, **423**, 705–714.
5 F.-X. Coudert, *Chem. Mater.*, 2015, **27**, 1905–1916.
6 S. Krause, V. Bon, I. Senkovska, U. Stoeck, D. Wallacher, D. M. Többens, S. Zander, R. S. Pillai, G. Maurin, F.-X. Coudert and S. Kaskel, *Nature*, 2016, **532**, 348–352.
7 A. U. Ortiz, A. Boutin, A. H. Fuchs and F.-X. Coudert, *Phys. Rev. Lett.*, 2012, **109**, 195502.
8 S. Horike, S. Shimomura and S. Kitagawa, *Nat. Chem.*, 2009, **1**, 695–704.
9 A. Schneemann, V. Bon, I. Schwedler, I. Senkovska, S. Kaskel and R. A. Fischer, *Chem. Soc. Rev.*, 2014, **43**, 6062–6096.
10 L. Vanduyfhuys, S. M. J. Rogge, J. Wieme, S. Vandenbrande, G. Maurin, M. Waroquier and V. Van Speybroeck, *Nat. Commun.*, 2018, **9**, 204.
11 K. T. Butler, A. Walsh, A. K. Cheetham and G. Kieslich, *Chem. Sci.*, 2016, **7**, 6316–6324.
12 K. T. Butler, J. M. Frost, J. M. Skelton, K. L. Svane and A. Walsh, *Chem. Soc. Rev.*, 2016, **45**, 6138–6146.
13 F.-X. Coudert and A. H. Fuchs, *Coord. Chem. Rev.*, 2016, **307**, 211–236.
14 A. L. Goodwin, *Nat. Commun.*, 2019, **10**, 4461.
15 Y. Sakata, S. Furukawa, M. Kondo, K. Hirai, N. Horike, Y. Takashima, H. Uehara, N. Louvain, M. Meilikhov, T. Tsuruoka, S. Isoda, W. Kosaka, O. Sakata and S. Kitagawa, *Science*, 2013, **339**, 193–196.
16 H. Miura, V. Bon, I. Senkovska, S. Ehrling, S. Watanabe, M. Ohba and S. Kaskel, *Dalton Trans.*, 2017, **46**, 14002–14011.
17 S. Krause, V. Bon, I. Senkovska, D. M. Többens, D. Wallacher, R. S. Pillai, G. Maurin and S. Kaskel, *Nat. Commun.*, 2018, **9**, 1573.
18 S. Wannapaiboon, A. Schneemann, I. Hante, M. Tu, K. Epp, A. L. Semrau, C. Sternemann, M. Paulus, S. J. Baxter, G. Kieslich and R. A. Fischer, *Nat. Commun.*, 2019, **10**, 346.
19 T. Kundu, M. Wahiduzzaman, B. B. Shah, G. Maurin and D. Zhao, *Angew. Chem., Int. Ed.*, 2019, **58**, 8073–8077.

20 S. Ehrling, I. Senkovska, V. Bon, J. D. Evans, P. Petkov, Y. Krupskaya, V. Kataev, T. Wulf, A. Krylov, A. Vtyurin, S. Krylova, S. Adichtchev, E. Slyusareva, M. S. Weiss, B. Büchner, T. Heine and S. Kaskel, *J. Mater. Chem. A*, 2019, **7**, 21459–21475.
21 S. O. Odoh, C. J. Cramer, D. G. Truhlar and L. Gagliardi, *Chem. Rev.*, 2015, **115**, 6051–6111.
22 S. M. J. Rogge, A. Bavykina, J. Hajek, H. Garcia, A. I. Olivos-Suarez, A. Sepúlveda-Escribano, A. Vimont, G. Clet, P. Bazin, F. Kapteijn, M. Daturi, E. V. Ramos-Fernandez, F. X. Llabrés i Xamena, V. Van Speybroeck and J. Gascon, *Chem. Soc. Rev.*, 2017, **46**, 3134–3184.
23 S. Bureekaew, S. Amirjalayer, M. Tafipolsky, C. Spickermann, T. K. Roy and R. Schmid, *Phys. Status Solidi B*, 2013, **250**, 1128–1141.
24 H. Fang, H. Demir, P. Kamakoti and D. S. Sholl, *J. Mater. Chem. A*, 2014, **2**, 274–291.
25 L. Vanduyfhuys, S. Vandenbrande, T. Verstraelen, R. Schmid, M. Waroquier and V. Van Speybroeck, *J. Comput. Chem.*, 2015, **36**, 1015–1027.
26 J. Heinen and D. Dubbeldam, *Wiley Interdiscip. Rev.: Comput. Mol. Sci.*, 2018, **8**, e1363.
27 J. Keupp and R. Schmid, *Adv. Theory Simul.*, 2019, **2**, 1900117.
28 S. M. J. Rogge, M. Waroquier and V. Van Speybroeck, *Nat. Commun.*, 2019, **10**, 4842.
29 J. P. Dürholt, R. Galvelis and R. Schmid, *Dalton Trans.*, 2016, **45**, 4370–4379.
30 L. Valenzano, B. Civalleri, S. Chavan, S. Bordiga, M. H. Nilsen, S. Jakobsen, K. P. Lillerud and C. Lamberti, *Chem. Mater.*, 2011, **23**, 1700–1718.
31 C. A. Trickett, K. J. Gagnon, S. Lee, F. Gándara, H.-B. Bürgi and O. M. Yaghi, *Angew. Chem., Int. Ed.*, 2015, **54**, 11162–11167.
32 G. C. Shearer, S. Chavan, S. Bordiga, S. Svelle, U. Olsbye and K. P. Lillerud, *Chem. Mater.*, 2016, **28**, 3749–3761.
33 W. Zhang, M. Kauer, P. Guo, S. Kunze, S. Cwik, M. Muhler, Y. Wang, K. Epp, G. Kieslich and R. A. Fischer, *Eur. J. Inorg. Chem.*, 2017, **2017**, 925–931.
34 O. Kozachuk, M. Meilikhov, K. Yusenko, A. Schneemann, B. Jee, A. V. Kuttatheyil, M. Bertmer, C. Sternemann, A. Pöppl and R. A. Fischer, *Eur. J. Inorg. Chem.*, 2013, **2013**, 4546–4557.
35 M. J. Cliffe, W. Wan, X. Zou, P. A. Chater, A. K. Kleppe, M. G. Tucker, H. Wilhelm, N. P. Funnell, F.-X. Coudert and A. L. Goodwin, *Nat. Commun.*, 2014, **5**, 4176.
36 S. Diring, S. Furukawa, Y. Takashima, T. Tsuruoka and S. Kitagawa, *Chem. Mater.*, 2010, **22**, 4531–4538.
37 Z. Fang, J. P. Dürholt, M. Kauer, W. Zhang, C. Lochenie, B. Jee, B. Albada, N. Metzler-Nolte, A. Pöppl, B. Weber, M. Muhler, Y. Wang, R. Schmid and R. A. Fischer, *J. Am. Chem. Soc.*, 2014, **136**, 9627–9636.
38 Y. Liu, J.-H. Her, A. Dailly, A. J. Ramirez-Cuesta, D. A. Neumann and C. M. Brown, *J. Am. Chem. Soc.*, 2008, **130**, 11813–11818.
39 N. Kavoosi, V. Bon, I. Senkovska, S. Krause, C. Atzori, F. Bonino, J. Pallmann, S. Paasch, E. Brunner and S. Kaskel, *Dalton Trans.*, 2017, **46**, 4685–4695.
40 T. D. Bennett, T. K. Todorova, E. F. Baxter, D. G. Reid, C. Gervais, B. Bueken, B. Van de Voorde, D. De Vos, D. A. Keen and C. Mellot-Draznieks, *Phys. Chem. Chem. Phys.*, 2016, **18**, 2192–2201.

41 K. W. Chapman, G. J. Halder and P. J. Chupas, *J. Am. Chem. Soc.*, 2009, **131**, 17546–17547.
42 T. D. Bennett and A. K. Cheetham, *Acc. Chem. Res.*, 2014, **47**, 1555–1562.
43 R. Gaillac, P. Pullumbi, K. A. Beyer, K. W. Chapman, D. A. Keen, T. D. Bennett and F.-X. Coudert, *Nat. Mater.*, 2017, **16**, 1149–1154.
44 J. M. Tuffnell, C. W. Ashling, J. Hou, S. Li, L. Longley, M. L. Ríos Gómez and T. D. Bennett, *Chem. Commun.*, 2019, **55**, 8705–8715.
45 R. Ameloot, F. Vermoortele, J. Hofkens, F. C. De Schryver, D. E. De Vos and M. B. J. Roeffaers, *Angew. Chem., Int. Ed.*, 2013, **52**, 401–405.
46 Z. Fang, B. Bueken, D. E. De Vos and R. A. Fischer, *Angew. Chem., Int. Ed.*, 2015, **54**, 7234–7254.
47 M. J. Cliffe, J. A. Hill, C. A. Murray, F.-X. Coudert and A. L. Goodwin, *Phys. Chem. Chem. Phys.*, 2015, **17**, 11586–11592.
48 J. Ren, M. Ledwaba, N. M. Musyoka, H. W. Langmi, M. Mathe, S. Liao and W. Pang, *Coord. Chem. Rev.*, 2017, **349**, 169–197.
49 W. G. Noid, *J. Chem. Phys.*, 2013, **139**, 090901.
50 H. I. Ingólfsson, C. A. Lopez, J. J. Uusitalo, D. H. de Jong, S. M. Gopal, X. Periole and S. J. Marrink, *Wiley Interdiscip. Rev.: Comput. Mol. Sci.*, 2014, **4**, 225–248.
51 N. Singh and W. Li, *Int. J. Mol. Sci.*, 2019, **20**, 3774.
52 R. Semino, J. P. Dürholt, R. Schmid and G. Maurin, *J. Phys. Chem. C*, 2017, **121**, 21491–21496.
53 S. J. Marrink and D. P. Tieleman, *Chem. Soc. Rev.*, 2013, **42**, 6801–6822.
54 T. Loiseau, C. Serre, C. Huguenard, G. Fink, F. Taulelle, M. Henry, T. Bataille and G. Férey, *Chem.–Eur. J.*, 2004, **10**, 1373–1382.
55 S. S.-Y. Chui, S. M.-F. Lo, J. P. H. Charmant, A. G. Orpen and I. D. Williams, *Science*, 1999, **283**, 1148–1150.
56 J. H. Cavka, S. Jakobsen, U. Olsbye, N. Guillou, C. Lamberti, S. Bordiga and K. P. Lillerud, *J. Am. Chem. Soc.*, 2008, **130**, 13850–13851.
57 W. G. Noid, J.-W. Chu, G. S. Ayton, V. Krishna, S. Izvekov, G. A. Voth, A. Das and H. C. Andersen, *J. Chem. Phys.*, 2008, **128**, 244114.
58 S. M. J. Rogge, J. Wieme, L. Vanduyfhuys, S. Vandenbrande, G. Maurin, T. Verstraelen, M. Waroquier and V. Van Speybroeck, *Chem. Mater.*, 2016, **28**, 5721–5732.
59 S. M. J. Rogge, M. Waroquier and V. Van Speybroeck, *Acc. Chem. Res.*, 2018, **51**, 138–148.
60 E. B. Tadmor and R. E. Miller, *Modeling Materials: Continuum, Atomistic and Multiscale Techniques*, Cambridge University Press, New York, 2011.
61 S. M. J. Rogge, L. Vanduyfhuys, A. Ghysels, M. Waroquier, T. Verstraelen, G. Maurin and V. Van Speybroeck, *J. Chem. Theory Comput.*, 2015, **11**, 5583–5597.
62 C. D. Christ and W. F. van Gunsteren, *J. Chem. Phys.*, 2007, **126**, 184110.
63 J. C. Tan, T. D. Bennett and A. K. Cheetham, *Proc. Natl. Acad. Sci. U. S. A.*, 2010, **107**, 9938–9943.
64 P. Z. Moghadam, S. M. J. Rogge, A. Li, C.-M. Chow, J. Wieme, N. Moharrami, M. Aragones-Anglada, G. Conduit, D. A. Gomez-Gualdron, V. Van Speybroeck and D. Fairen-Jimenez, *Matter*, 2019, **1**, 219–234.
65 J. Hou, C. W. Ashling, S. M. Collins, A. Krajnc, C. Zhou, L. Longley, D. N. Johnstone, P. A. Chater, S. Li, M.-V. Coulet, P. L. Llewellyn, F.-X. Coudert, D. A. Keen, P. A. Midgley, G. Mali, V. Chen and T. D. Bennett, *Nat. Commun.*, 2019, **10**, 2580.